

AD-A179 782

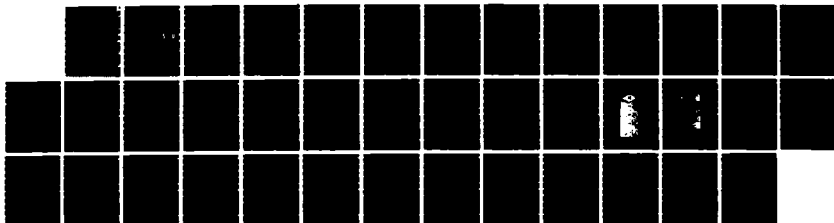
INTERNAL FRACTURE IN AN ELASTOMER CONTAINING A RIGID
INCLUSION(U) AKRON UNIV OH INST OF POLYMER SCIENCE
K CHO ET AL MAY 87 TR-8 N00014-85-K-0222

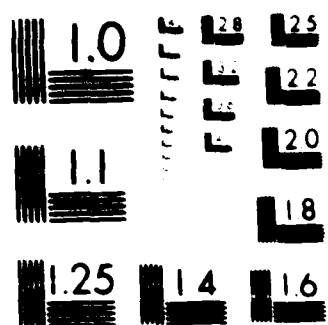
1/1

UNCLASSIFIED

F/G 11/10

NL





AD-A179 782

DTIC FILE CODE

(12)

OFFICE OF NAVAL RESEARCH

Contract N00014-85-K-0222

Project NR 092-555

Technical Report No. 8

INTERNAL FRACTURE IN AN ELASTOMER CONTAINING
A RIGID INCLUSION

by

K. Cho, A. N. Gent and P. S. Lam*

Institute of Polymer Science
The University of Akron
Akron, Ohio 44325

May, 1987

Reproduction in whole or in part is permitted for

any purpose of the United States Government

Approved for Public Release; Distribution Unrestricted

*Research Division, The Goodyear Tire & Rubber Company, Akron, Ohio 44316



87 4 29 006

REPORT DOCUMENTATION PAGE		READ INSTRUCTIONS BEFORE COMPLETING FORM
1. REPORT NUMBER Technical Report No. 8	2. GOVT ACCESSION NO.	3. RECIPIENT'S CATALOG NUMBER
4. TITLE (and Subtitle) Internal Fracture in an Elastomer Containing a Rigid Inclusion		5. TYPE OF REPORT & PERIOD COVERED Technical Report
		6. PERFORMING ORG. REPORT NUMBER
7. AUTHOR(s) K. Cho, A. N. Gent and P. S. Lam		8. CONTRACT OR GRANT NUMBER(s) N00014-85-K-0222
9. PERFORMING ORGANIZATION NAME AND ADDRESS Institute of Polymer Science The University of Akron Akron, Ohio 44325		10. PROGRAM ELEMENT, PROJECT, TASK AREA & WORK UNIT NUMBERS NR 092-555
11. CONTROLLING OFFICE NAME AND ADDRESS Office of Naval Research Power Program Arlington, VA 22217		12. REPORT DATE May, 1987
		13. NUMBER OF PAGES 37
14. MONITORING AGENCY NAME & ADDRESS (if different from Controlling Office)		15. SECURITY CLASS. (of this report) Unclassified
		15a. DECLASSIFICATION/DOWNGRADING SCHEDULE
16. DISTRIBUTION STATEMENT (of this Report) According to attached distribution list. Approved for public release; distribution unrestricted.		
17. DISTRIBUTION STATEMENT (of the abstract entered in Block 20, if different from Report)		
18. SUPPLEMENTARY NOTES Submitted for publication in: Journal of Materials Science		
19. KEY WORDS (Continue on reverse side if necessary and identify by block number) Cavitation, Composites, Elastomers, Fracture, Inclusions, Reinforcement, Strength, Voids.		
20. ABSTRACT (Continue on reverse side if necessary and identify by block number) Rubber blocks were prepared with thin glass rods in their centers, firmly bonded to the surrounding rubber. A tensile stress applied to the ends of a block in the direction of the rod axis induced the sudden formation of voids in the rubber near the flat ends of the rod. (1-5)		

20. Abstract (Continued)

Approximate values of the local stresses have been calculated by FEM, assuming linear elastic behavior. Voids were found to form when and where the local dilatant stress $-P$ (negative hydrostatic pressure) exceeded the magnitude of Young's modulus E for the rubber. A precursor void in a highly-elastic solid would expand indefinitely under these circumstances, so that fracture seems to be the result of an elastic instability. The applied stress at which voids appeared was of the same order as E for short rods, or for a butt joint between a rod and a rubber cylinder of the same diameter, but it became extremely small when the rod was thin compared to the block in which it was embedded, and relatively long. Under these circumstances the local dilatant stress is calculated to be a large multiple of the applied tensile stress. *Key words*

Accession For	
NTIS CRA&I	<input checked="" type="checkbox"/>
DTIC TAB	<input type="checkbox"/>
Unannounced	<input type="checkbox"/>
Justification	
By	
Distribution/	
Availability Codes	
Dist	Avail and/or Special
A-1	



1. Introduction

Composites, consisting of high-modulus fibers or particles embedded in a softer matrix, are an important class of structural materials. But the edges and surfaces of the inclusions can act as sites of dangerous stress concentrations and cause internal failure of the softer matrix material. Most previous work has dealt with the problem of stress transfer between the inclusion and the matrix (1-6); few studies of matrix fracture induced by the inclusion have been reported (7-9).

One particular mode of fracture is considered here. Termed cavitation, it consists of the sudden appearance of a void within an elastomeric solid when the triaxial tension $-p$ (negative hydrostatic pressure) at that point reaches a critical value, denoted P_c . This process is regarded as the unstable elastic expansion of a pre-existing void, too small to be readily detected, followed by its growth as a running crack when the maximum elongation of the material has been exceeded (7). Growth of the void stops when it becomes large enough to alleviate the triaxial tension which gave rise to it.

In a previous study, cavitation was observed in an elastomeric matrix containing a rigid spherical inclusion (9). Voids formed near the surface of the inclusion in the direction of the applied tension when the magnitude of the far-field tensile stress reached a critical value, t_c . For large inclusions, having a diameter d of 5 mm or more, the critical applied

stress was found to be about $E/2$, where E is Young's modulus of the matrix elastomer. This corresponds to a triaxial tension at the poles of the inclusion of approximately E , in good agreement with the theoretical value for cavitation by the unbounded expansion of the precursor void in an incompressible highly-elastic solid, i.e., $5E/6$ (7).

Larger stresses were found to be necessary to cause cavitation in the vicinity of smaller inclusions, although it is not at all clear why this is so. An empirical relation was found to hold (9):

$$t_c = (5E/12) + k/d^2$$

where k is an experimentally-determined constant, 25 to 40 kPa.m².

We turn now to the phenomenon of cavitation near the flat end surfaces of a rigid rod, embedded in an elastomeric matrix which is subjected at infinity to a simple tensile stress in the direction of the rod axis. Two special cases are emphasized: the short rod, corresponding to a thin disk in the interior of the elastomeric material; and a rod that is long in comparison with the lateral dimensions of the sample containing it, so that it is effectively semi-infinite in length.

The general nature of the observed failures is described first and then some numerical values of the failure stresses are given and compared with theoretical estimates of cavitation stresses. In order to make these comparisons, values of the triaxial tension set up near the end surfaces of the rods have been computed using a finite-element method, assuming that the matrix material is linearly elastic and incompressible, and that the inclusion is rigid and perfectly bonded to the matrix.

2. Experimental

Preparation of test-pieces

Inclusions were prepared by cutting and polishing soda-lime glass rods of varied length and having diameters in the range 0.6 to 2.2 mm. Care was taken to ensure that the end surfaces were flat and that the edges were sharp. The rods were treated with a dilute solution of vinyltriethoxysilane in water, using acetic acid as a catalyst, to obtain good bonding later to the elastomeric matrix (10).

After dipping in the treatment solution, the rods were heated for 30 min at 110°C to promote reaction of the silane with the glass surface. They were then placed in the center of a long rectangular strip of natural rubber (SMR-5, Rubber Research Institute of Malaysia) containing 2 per cent by weight of dicumyl peroxide. The composite specimen was placed in a heated press for 60 min at 150°C so that decomposition of the peroxide took place and the rubber became cross-linked, changing from a soft plastic material into a highly-elastic solid. Simultaneously, a strong bond was formed with the glass inclusion.

The value of Young's modulus for the crosslinked rubber was found to be 1.5 MPa, much lower than that of glass, about 10 GPa. Thus, the rod-like inclusions can be treated as rigid in comparison with the rubber.

Measurement of critical stress $\underline{t_c}$

A sketch of a test specimen is shown in Figure 1.

The thickness \underline{T} of the rubber block was generally chosen to be at least three times the diameter \underline{d} of the centrally-located rod and the width \underline{W} was made generally about twice as large as \underline{T} . Thus, the rod was effectively located within a thick rubber block. Nevertheless, the rubber was sufficiently transparent to permit visual inspection of the region around the rod ends with a low-power microscope through the rubber.

This region was continuously monitored while the rubber was being stretched at a strain rate of about $4 \times 10^{-4} \text{ s}^{-1}$ (measured on that portion of the sample that did not contain the inclusion). Some typical observations are described in the following section. A measurement of the tensile strain \underline{e} in the part of the sample away from the inclusion was made at the moment when the first void suddenly appeared at the rod end. This measurement was made by means of an ink grid applied to the rubber surface in the unstrained state. The critical strain level was then converted into a corresponding critical value of the applied stress \underline{t} from the previously-determined relation between tensile stress and extension for the rubber.

3. Experimental results and discussion

Qualitative observations

The development of internal fractures is shown in Figure 2 for a specimen containing a short glass rod, $L/d = 1$. When the far-field tensile strain reached a critical value of about 100 per cent, a small cavity appeared close to one flat end of the rod and close to the rod edge. Then at a somewhat higher strain level a second cavity appeared near the center of the flat surface of the rod and another cavity appeared at the other end of the rod, again near the edge. On stretching further, other cavities appeared and linked up, at least partially, to form large pointed voids at both ends of the rod, Figure 2.

Quite similar processes were observed with a long glass rod, $L/d = 5$, Figure 3, although the critical value of the far-field tensile strain was somewhat smaller in this case, about 60 per cent. It is again noteworthy that the first cavities appeared towards the edges of the flat end surfaces, followed by cavities in the central region at somewhat higher strain levels.

Proposed mechanism of failure

A proposed sequence of failure events corresponding to the observed development of voids is shown in Figure 4. At first, a hypothetical precursor void, too small to see, expands under the large triaxial tension $-P$ acting near the flat surface of the rod, Figure 4a. When the degree of expansion exceeds

the maximum extensibility of the rubber the void wall will split apart and the cavity will grow further by tearing, Figures 4b, 4c, to reach a visible size. At somewhat higher stresses, other voids, situated in less favorable locations or of smaller size, will be also induced to grow into large,

visible cavities, Figure 4d. However, they are still at this stage entirely surrounded by rubber. Although they are formed close to the surface of the inclusion, where the dilatant stress is largest, they do not make contact with the rigid surface. They can be distinguished from voids formed by detachment from weakly-bonded inclusions by the characteristic "convex lens" shape of the regions between the void and the surface of the inclusion. Indeed, it is sometimes possible to see the thin layer of rubber remaining between the void and the inclusion. However, at still larger stresses the shape of that part of the void in close proximity to the inclusion surface undergoes a marked change, Figure 4e, which is attributed to detachment from the inclusion and rupture of the layer of rubber separating the void from it. Finally, the cavities link up by further detachment and tearing apart of the layers of rubber separating them, Figure 4f. These several stages can be recognized in Figures 2 and 3.

It is noteworthy that the voids do not lead directly to fracture of the specimen. Because they are oriented in the direction of the applied stress they can grow to a substantial size without becoming unstable.

Cavitation stresses

We now turn to the critical conditions for formation of the first visible voids. Values of the applied stress \underline{t}_c at which the first void appeared near the rod end are plotted in Figure 5 against the length \underline{L} of the rod for two different widths \underline{W} of the rubber block. The rod diameter \underline{d} was relatively small in comparison with the width or thickness of the rubber block so that when the rod length \underline{L} was also small it became a small thin disk located in the center of a large rubber block with its axis parallel to the direction of the applied tension. Under these circumstances the critical applied stress for cavitation was found to be about 1.75 MPa, and independent of the width or thickness of the rubber block.

When the rod was longer, however, the critical stress was appreciably lower and it now depended upon the width and thickness of the rubber block, Figure 5. When the block had a large cross-section, the critical stress for void formation at the end of a long rod was small, and vice versa.

The two extreme cases; a short rod or small disk in the center of a thick rubber block, and a long rod embedded in a block of varied width and thickness; are now considered separately.

Short rod or disk inclusions

Values of the critical applied stress were determined for short-rod inclusions ($L/d \approx 1$) and for small glass cubes arranged so that two of the faces were normal to the far-field tensile stress. The results were virtually identical and independent of the length or diameter over the range investigated, 0.6 to 2.2 mm, as shown in Figure 6. The mean value of the true far-field cavitation stress t_c (given by $(1 + e)t_c$ where t_c is the engineering critical stress, i.e., the applied force per unit of undeformed cross-sectional area) was 1.42 MPa.

From finite-element calculations, described in the Appendix, the dilatant stress $-P$ acting in the surface plane of a thin rigid disk, located at the center of a thick block of an incompressible linearly-elastic material was found to be substantially uniform over the surface of the disk, out to a radius $r = 0.85(d/2)$ and approximately equal to the applied far-field tensile stress, Figure 7. Thus, the criterion for formation of the first cavity appears to be that the local dilatant stress, 1.42 MPa in the present case, reaches a value of the same order as Young's modulus E for the elastomer; 1.5 MPa for the natural rubber compound employed here. This is in good agreement with the critical condition for the unbounded elastic expansion of a small spherical cavity in a block of a highly-elastic solid (7).

It is interesting to compare cavitation near the flat surface of a disk or cube with the corresponding process near a rigid spherical inclusion. Results for spherical inclusions of various diameters, taken from an earlier investigation (9), are shown in Figure 6 for comparison. The critical stresses for spherical inclusions depended strongly upon the size of the

inclusions. They were only in good accord with the theoretical prediction $-P \approx E$, corresponding to $\sigma_c \approx E/2$ for a spherical inclusion, when the diameter d was relatively large, several mm or greater. For smaller diameters, about 1 mm or so, the critical stress was about twice as large as predicted and it increased sharply as the diameter of the inclusion was reduced further, Figure 6.

This anomalous behavior might reflect the relatively small volume of material at the poles of a spherical inclusion that is subjected to a large dilatant stress, in comparison to that near the flat surface of a disk of similar diameter. If precursor voids of sufficient size to become elastically unstable when $-P \approx E$ are distributed sparsely, so that there are few or none in a volume of less than, say, 10^{-14} m^3 , then higher stresses would be needed to induce cavitation when the volume under a dilatant stress is as small as this. For a spherical inclusion having a diameter of 1 mm, the volume under a large dilatant stress is only of this order of magnitude. For a disk of the same diameter, the corresponding volume of rubber under a high dilatant stress is about 10^{-12} m^3 , several orders of magnitude larger, and precursor voids of sufficient size may then be plentiful.

Experiments with disks of much smaller diameter would be helpful to examine whether the critical stress for cavitation is then larger than predicted, in the same way that it is for spherical inclusions of about 1 mm in diameter.

Long rod inclusions

The experimental method used for studying cavitation near the flat end surface of a rod of semi-infinite length is shown in Figure 8. Wide ranges of width and thickness of the rubber block were employed. At one extreme, the

block had the same cross-section as the glass rod and was joined to it end-to-end as a butt joint. In this case, $W = d$. The other extreme case employed a rubber block having a width and thickness of about $10d$. Two different diameters of glass rod were used, about 0.6 and about 2.2 mm.

Measured values of the applied stress at which a cavity first appeared are plotted in Figure 9 against the ratio d/W of the rod diameter to the width and thickness of the square-sided block. Results are given for cavities which first appeared near the edge of the rod end surface, open points, and for cavities appearing near the center, filled-in points. Cavities at the edge generally formed first, at somewhat lower stresses.

The critical stresses were found to be independent of the diameter d of the rod, over the limited range studied, but they depended strongly upon the ratio d/W . For the butt-jointed test-piece, when $d/W = 1$, the true applied stress was about 5 MPa and the engineering applied stress was about 1.5 MPa for cavitation. At the other extreme, cavities formed at an applied stress of only about 0.3 MPa when the rod diameter was much smaller than the width and thickness of the rubber block, Figure 9.

Before discussing theoretical estimates of the cavitation stress, represented by the broken curves in Figure 9, it should be explained why, in this Figure, the results are given in terms of engineering stress instead of true stress. When the inclusion is small in comparison to the block in which it is embedded, the appropriate measure of far-field fracture stress is probably the true stress, as has been employed hitherto. In the present case, however, the long rod inclusion prevents the rubber surrounding it from undergoing a significant amount of extension and thus, almost up to the rod end, the rubber

block retains its original cross-section. In the rest of the rubber block, on the other hand, the rubber stretches considerably and its cross-sectional area decreases correspondingly. Because Poissonian contraction is inhibited at the rod end to a marked degree, the relevant "far-field" stress seems to be that calculated on the basis of the original cross-sectional area, i.e., the engineering stress $\underline{\sigma}$, rather than the true stress $\underline{\sigma}_t$ acting in that portion of the specimen that undergoes an unrestrained contraction in the cross-sectional area.

Using the finite-element method described in the Appendix, values of dilatant stress $-\underline{P}$ were computed as a function of radial distance \underline{r} for a plane in a cylindrical elastic block lying close to the flat end of a long embedded rigid rod. Again, the block was assumed to be incompressible and linearly-elastic. Results are shown in Figure 10 for a block having a diameter \underline{D} twice as large as that of the embedded rod, for planes at various distances \underline{z} away from the flat end of the rod. When \underline{z} is large, the dilatant stress is relatively uniform and given by $\underline{\sigma}/3$, where $\underline{\sigma}$ is the applied far-field stress. When \underline{z} is small, the dilatant stress is considerably larger and rises from a value of about 1.4 $\underline{\sigma}$ at the center of the rod end surface to a value of about 1.7 $\underline{\sigma}$ near the edge. The cause of possible inaccuracy arising at the rod edge from stress singularities and the relatively coarse mesh used in these computations, with the exception of $\underline{z}/\underline{d} = 1$, the rod radius $\underline{d}/2$, the dilatant stress in the vicinity of the rod edge has been taken at the radial distance, $\underline{r} = \sqrt{3}\underline{d}/2$, rather than at the corner or edge point, $\underline{r} = \underline{d}/2$. These results, together with those obtained at the center of the rod end surface, are plotted in Figure 11 as a function of the ratio of the rod diameter \underline{d} to the block diameter \underline{D} and the distance \underline{z} from the rod end to the plane of interest.

When the rod diameter is equal to that of the block, corresponding to a butt joint between a rigid rod and an elastic one, the results show that the

dilatant stress set up at the interface is approximately the same as the applied far-field tensile stress, except very near the edge where stress singularities dominate. When the rod is much smaller than the block in which it is embedded, the dilatant stress at the rod end is much larger than the far-field tensile stress at the center and even larger towards the edge of the rod end surface.

These results can be employed to calculate theoretical values for the applied stress at which cavitation takes place, on the assumption that the critical condition for cavitation is that the dilatant stress approaches the magnitude of Young's modulus $-P = E$. The broken curves in Figure 9 were obtained in this way from the relations given in Figure 11. They describe the experimentally-measured conditions for cavity formation with considerable success, over the whole range of rod and block dimensions. We conclude that dilatant stresses near the rod ends are, indeed, responsible for the observed failures, and that they take place when and where the dilatant stress approaches E in magnitude.

4. Conclusions

The following conclusions are obtained:

- (a) A characteristic internal fracture process, termed cavitation, is observed in a stretched elastomeric block containing a rigid disk or rod.
- (b) The critical applied stress at which cavities form is affected by the width and thickness of the rubber block and by the length of the rod. For a short rod, i.e., a disk, it is independent of the rod diameter and of the size of the rubber block in which it is embedded, and is approximately equal to Young's modulus E of the elastomer. For long rods, it is inversely proportional to the width and thickness of the rubber block and becomes quite small, less than $E/5$, when the width and thickness are 10X the rod diameter.
- (c) The first cavities form near the edges of the flat end surfaces of the rod. At higher stresses cavities also appear in the center, but still close to the interface.
- (d) Stress distributions near the rod surface have been calculated by finite element methods, assuming perfect bonding of an incompressible, linearly-elastic material.
- (e) The observed cavitation stresses are in satisfactory agreement in all cases with a simple fracture criterion: that voids ~~form~~ where, and when, the local dilatant stress $-P = E$. This is the same criterion that governs the unstable elastic expansion of a spherical void in a highly-elastic solid and suggests that invisibly-small precursor voids are plentiful in elastomeric solids.

References

1. H. L. Cox, Brit. J. Appl. Phys. 3 (1952) 72.
2. N. F. Dow, General Electric Co., Schenectady, N. Y., Report R635D 61 (1963).
3. D. M. Schuster and E. Scala, Trans. Metal. Soc. 230 (1964) 1635.
4. W. R. Tyson and G. W. Davies, Brit. J. Appl. Phys. 16 (1965) 199.
5. I. M. Allison and L. C. Holloway, Brit. J. Appl. Phys. 18 (1967) 979.
6. A. S. Carrara and F. J. McGarry, J. Comp. Mater. 2 (1968) 222.
7. A. N. Gent and P. B. Lindley, Proc. Roy. Soc. (London) A249 (1959) 195.
8. A. E. Oberth and R. S. Bruenner, Trans. Soc. Rheol. 9 (1965) 165.
9. A. N. Gent and B. Park, J. Mater. Sci. 19 (1984) 1947.
10. A. Ahagon and A. N. Gent, J. Polym. Sci. Polym. Phys. Ed. 13 (1975) 1285.
11. MARC Analysis Research Corporation.
12. L. R. Hermann, AIAA 3 (1965) 1896.

Appendix

Finite element analysis

Stress distributions within the rubber block were analyzed using a finite element method. The rubber block was treated as a long cylinder containing a long rigid rod or a thin rigid disk. The rod extended from one end of the rubber cylinder to its middle section. The length of rod was chosen to be thirty times its radius and the radius of the rubber cylinder was chosen to be one, two, or ten times the radius of the rod. In the case of the embedded disk, the radius of the rubber cylinder was taken to be ten times the radius of the disk, which was given a thickness (length) of zero. A uniform tensile stress was assumed to be applied at both ends of the rubber cylinder, of magnitude $E/100$, where E is Young's modulus of the rubber. The rubber was assumed to be linearly elastic and incompressible, with Poisson's ratio equal to 0.5. The rod and disk were assumed to be perfectly rigid.

The finite element model was analyzed using the MARC program (11). The incompressible restraint was enforced by the Herrmann variational principle (12) which treats the hydrostatic pressure as an independent variable.

The rubber matrix in the vicinity of the end of the rigid rod was mainly considered in the analysis, since fracture occurs in this region. Large stress gradients were expected; therefore, eight-noded quadrilateral axisymmetric elements with nine Gaussian integration points were used. There were ten equally-spaced elements in the radius direction, along the interface, with an element height of $0.01d$ where d is the rod diameter. The element height was increased gradually for element layers lying further away from the interface.

Perfect bonding was assumed to exist between the rigid rod and the matrix. Hence, the boundary conditions at the interface were set up to disallow relative

displacements between adjacent faces of the rigid rod and the matrix. The computer program calculated stresses in the axial, radial and hoop directions:

σ_{zz} , σ_{rr} , $\sigma_{\theta\theta}$. The dilatant stress, $-P = (\sigma_{zz} + \sigma_{rr} + \sigma_{\theta\theta})/3$, was evaluated at the center of each element.

Figure Legends

- Figure 1. Rubber block, containing a glass rod at its center, subjected to an applied tensile stress.
- Figure 2. Development of cavitation near a short rod inclusion, $L/d = 0.75$.
- Figure 3. Development of cavitation near a long rod inclusion, $L/D = 5$.
- Figure 4. Sketch of proposed development of internal failures from hypothetical precursor voids.
- (a) Elastic expansion of a precursor void
 - (b, c) Growth by tearing to a visible size
 - (d) Multiple cavities
 - (e) Detachment from the substrate
 - (f) Joining up by detachment or tearing
- Figure 5. Effect of length L of rod on the critical applied stress for cavitation for two different widths W of rubber block. Block thickness $T = 4.8$ mm. Rod diameter $d = 2.2$ mm.
- Figure 6. Critical stresses for cavitation near a short rod (\circ) or cube (\square) inclusion and near a spherical inclusion (\bullet) (9) vs diameter or width d of inclusion.
- Figure 7. Computed distribution of dilatant stress $-P$ near the surface of a thin rigid disk with its axis in the direction of the applied far-field tensile stress σ .
- Figure 8. Sketch of experimental arrangement for a rod of semi-infinite length.

Figure 9. Critical stresses σ_c for cavitation near the flat end of a rod of semi-infinite length vs the ratio d/W of rod diameter d to width W of the rubber block in which it is embedded. Squares, rod diameter $d = 0.6$ mm; circles, $d = 2.2$ mm. Crosses and broken curves, results obtained from FEM calculations, Figures 10 and 11, assuming that $-P_c = 0.75 E$.

Figure 10. Calculated distributions of dilatant stress $-P$ near the flat end of a long rigid rod of diameter d embedded in an elastic block of diameter $D = 2d$. The distance above the rod end is denoted by z . The far-field tensile stress is denoted by σ .

Figure 11. Calculated values of dilatant stress $-P$ near the flat end of an embedded rod vs the ratio of the rod diameter d to the diameter D of the rubber block in which it is embedded. The far-field tensile stress is denoted by σ . Upper curve, $-P$ calculated at $r = 0.85 (d/2)$; lower curve, $-P$ calculated at $r = 0$.

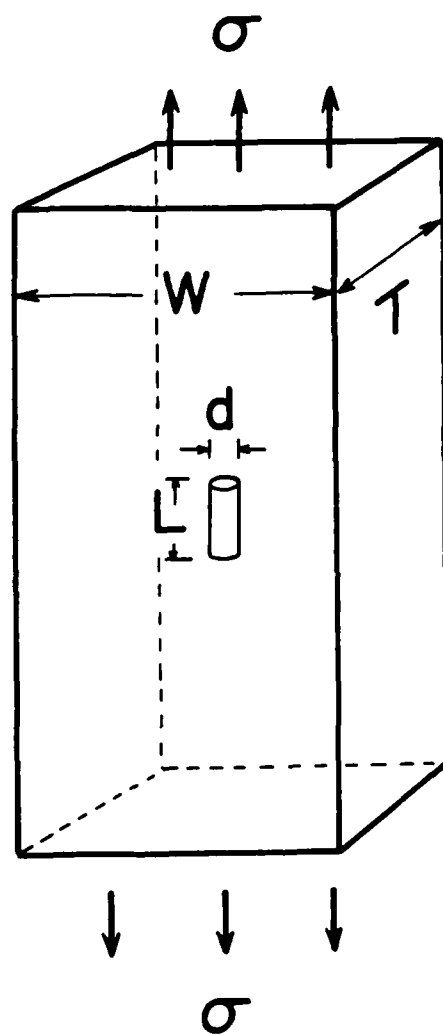


Figure 1

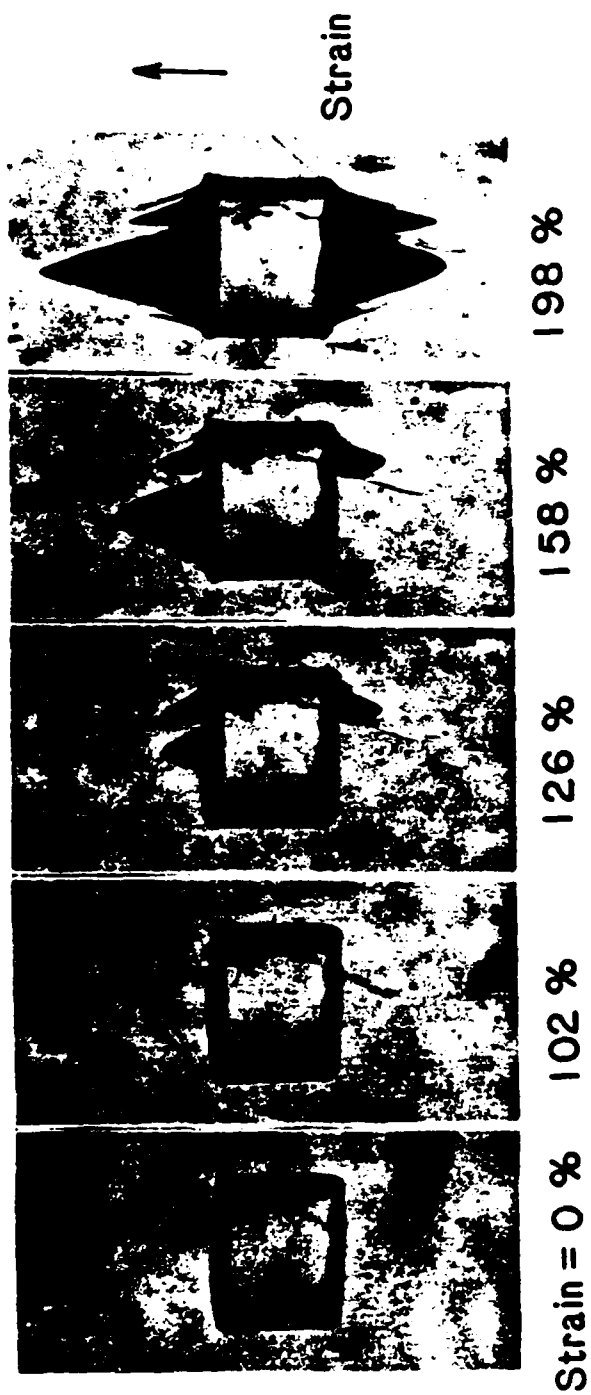


Figure 2

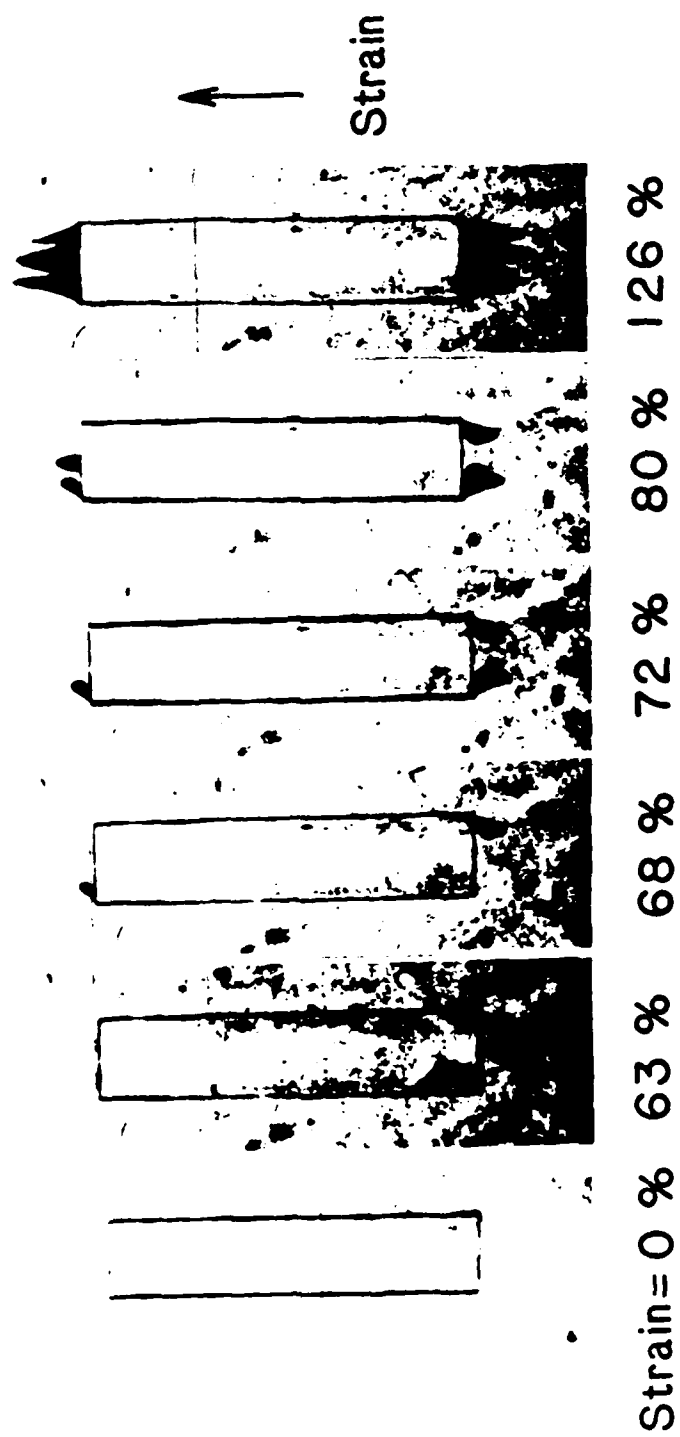


Figure 3

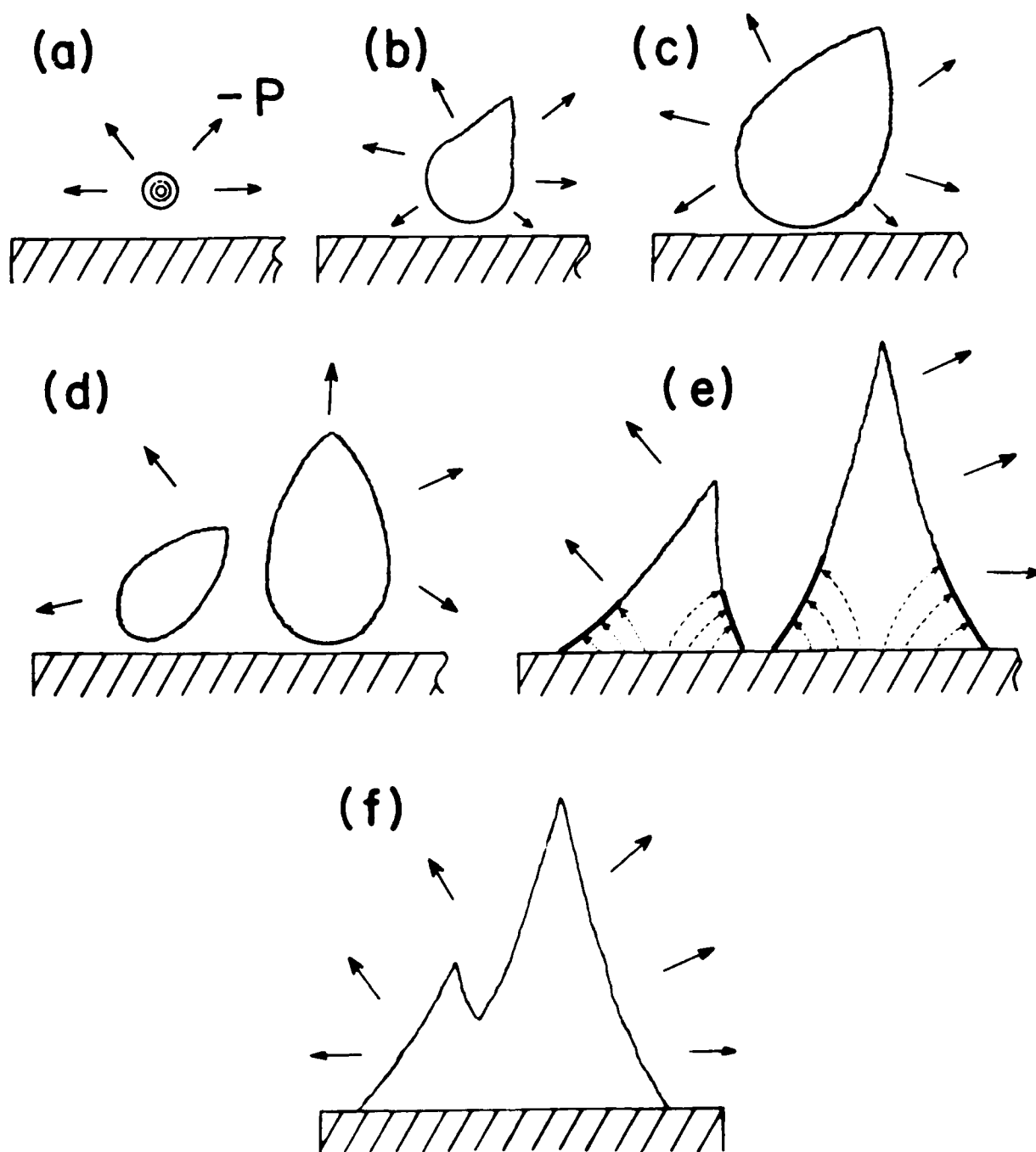


Figure 4

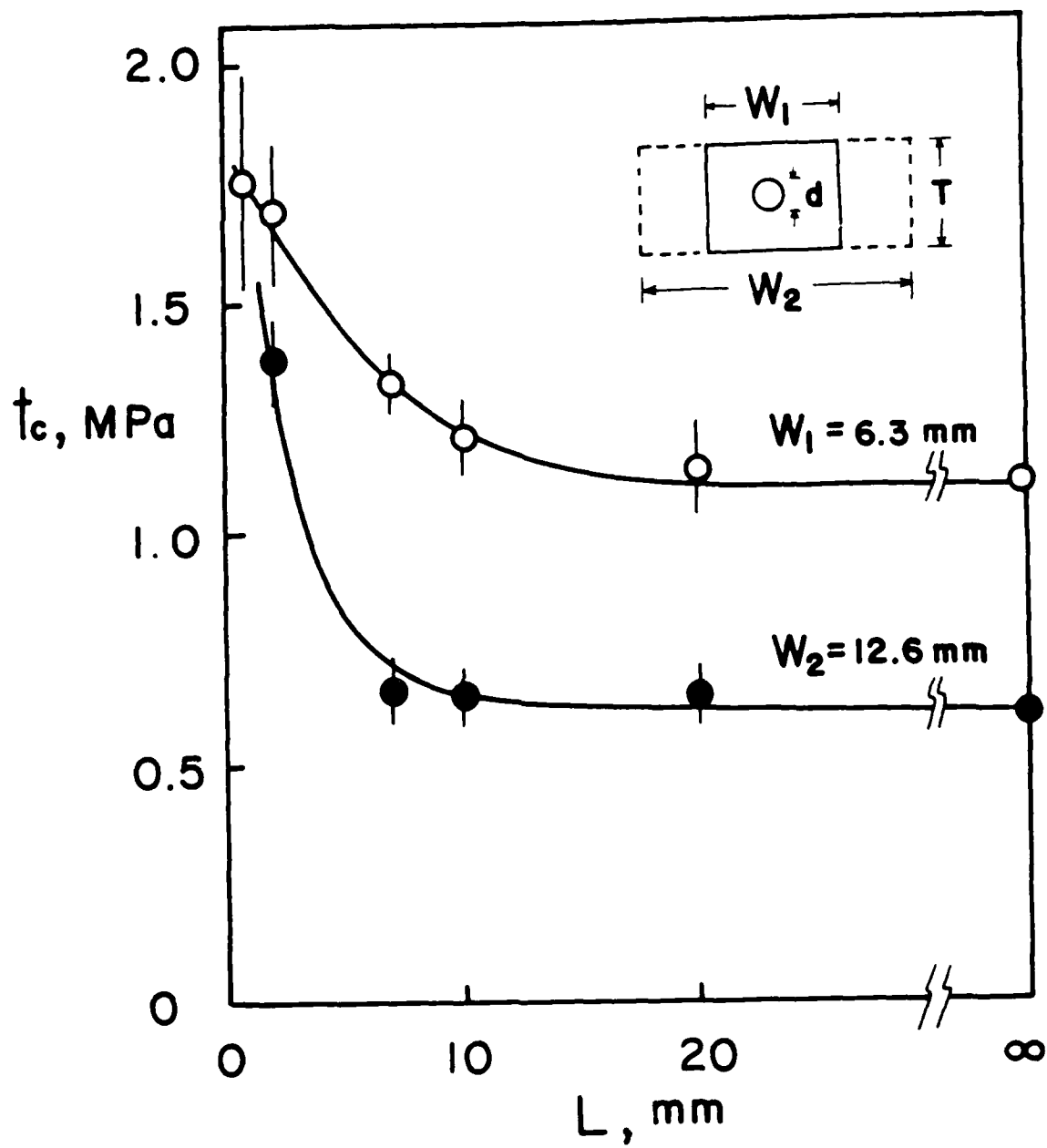


Figure 5

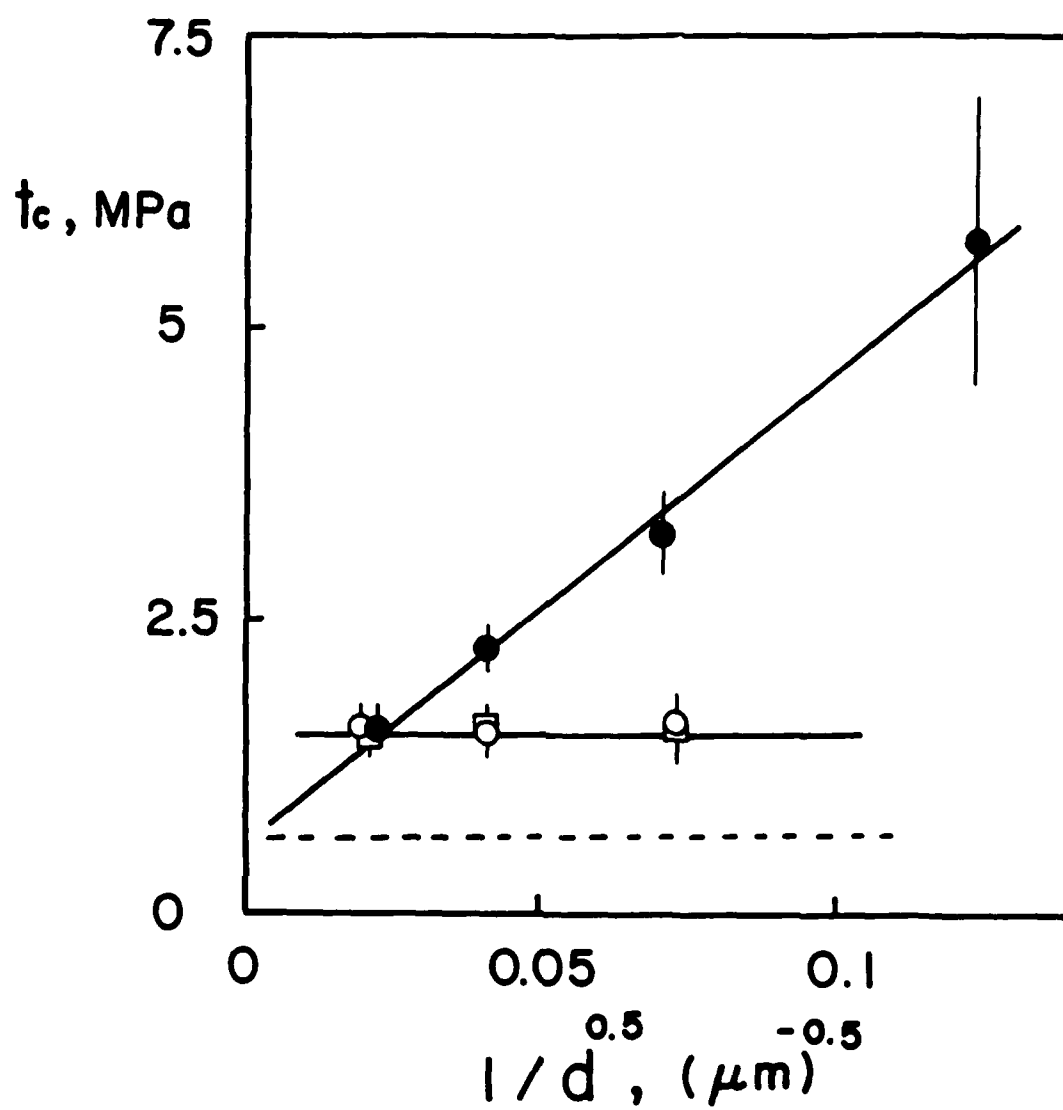
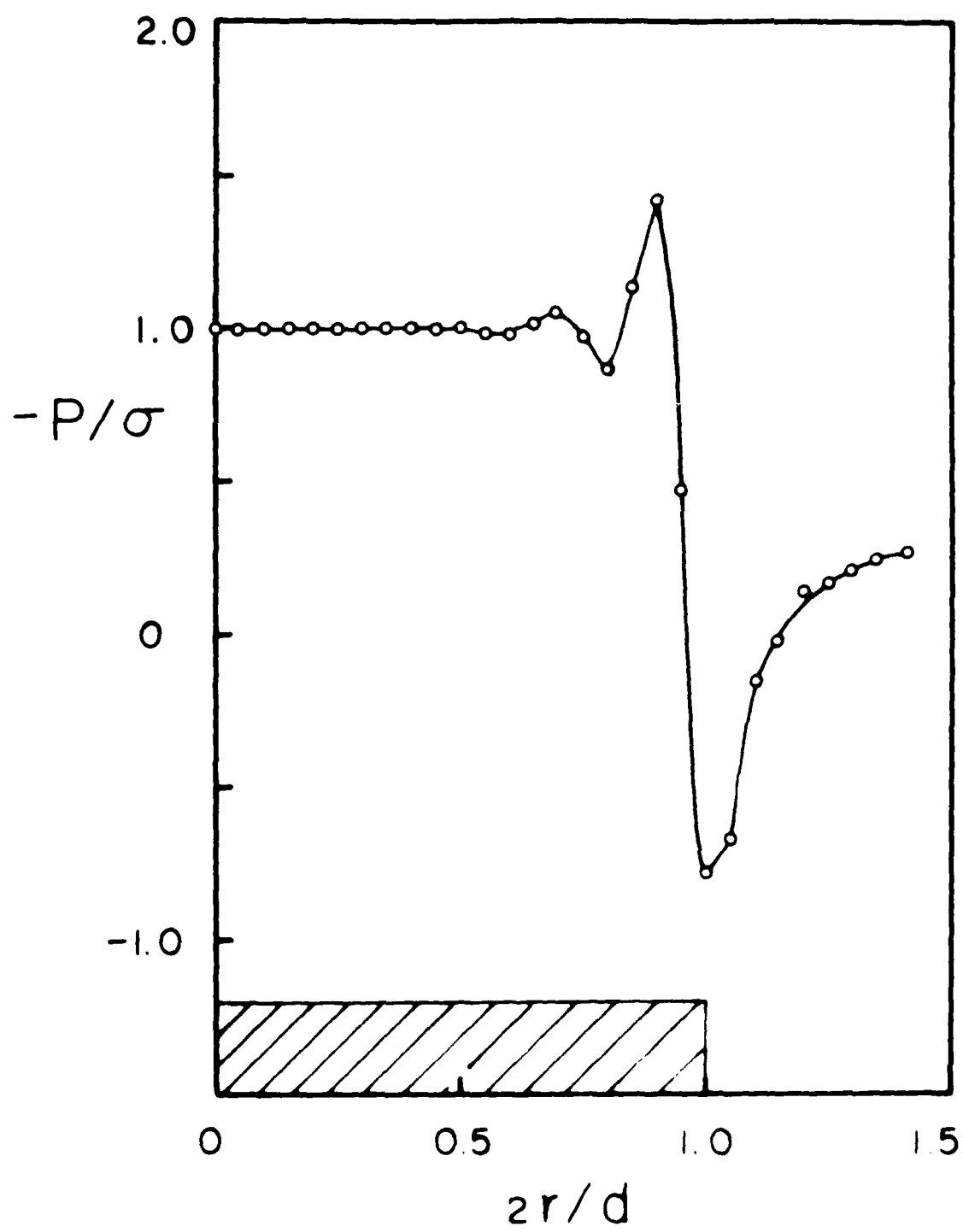
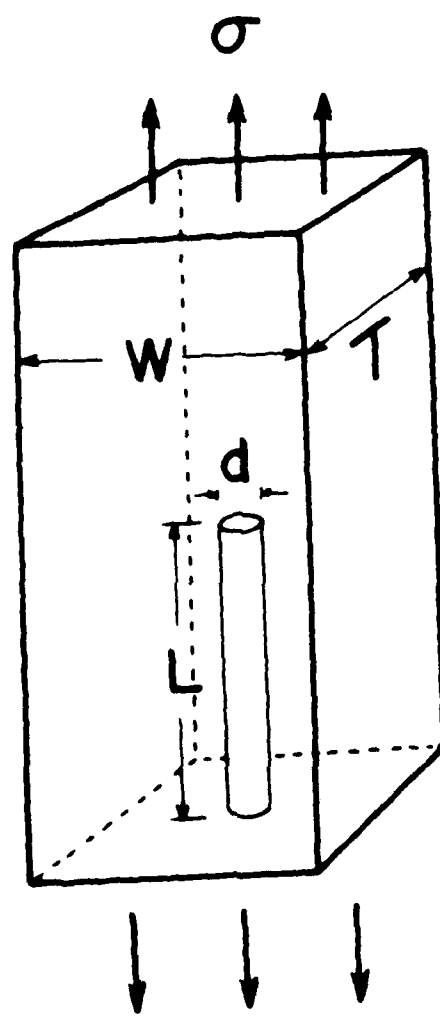


Figure 6





$$L \geq 30 d$$

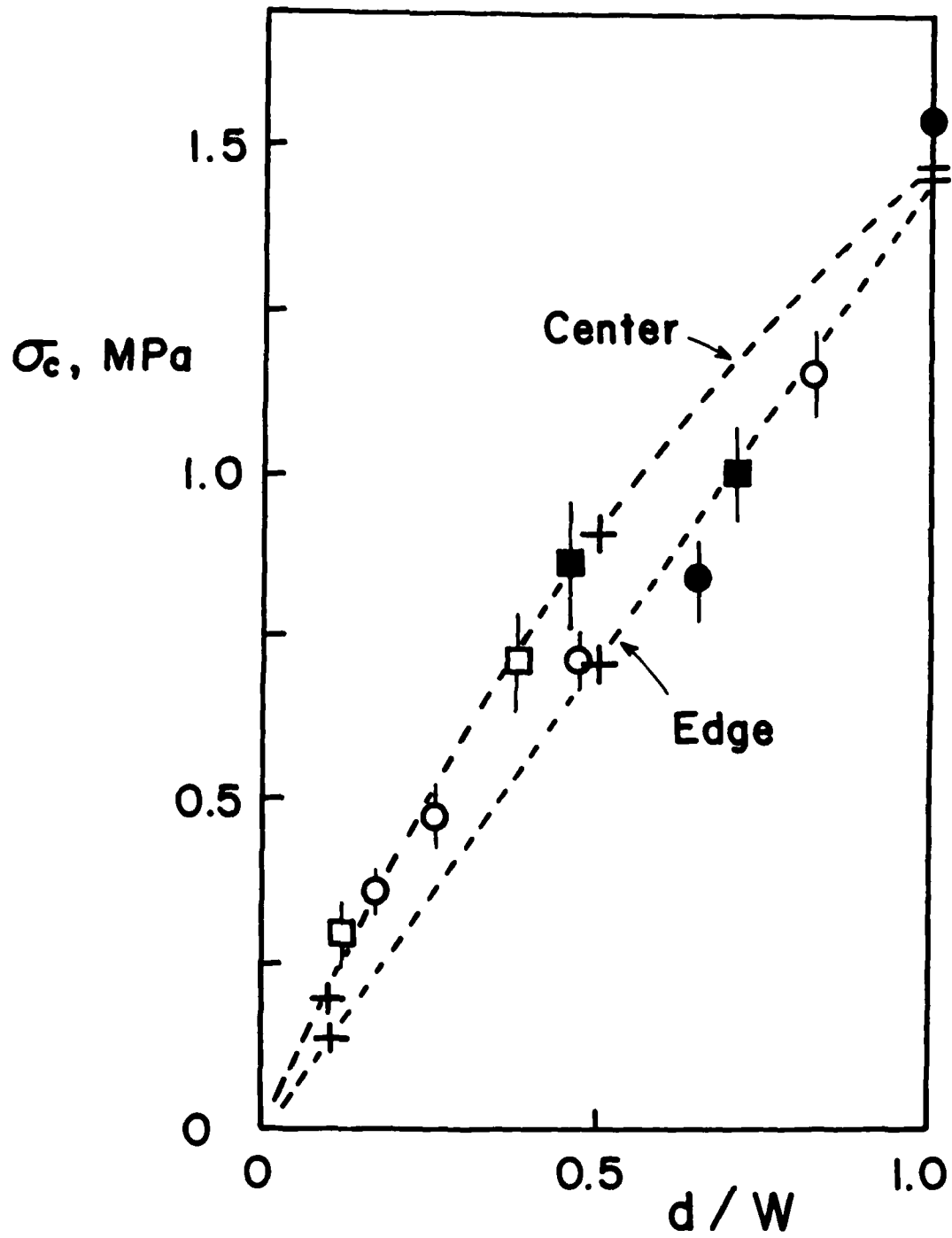


Figure 9

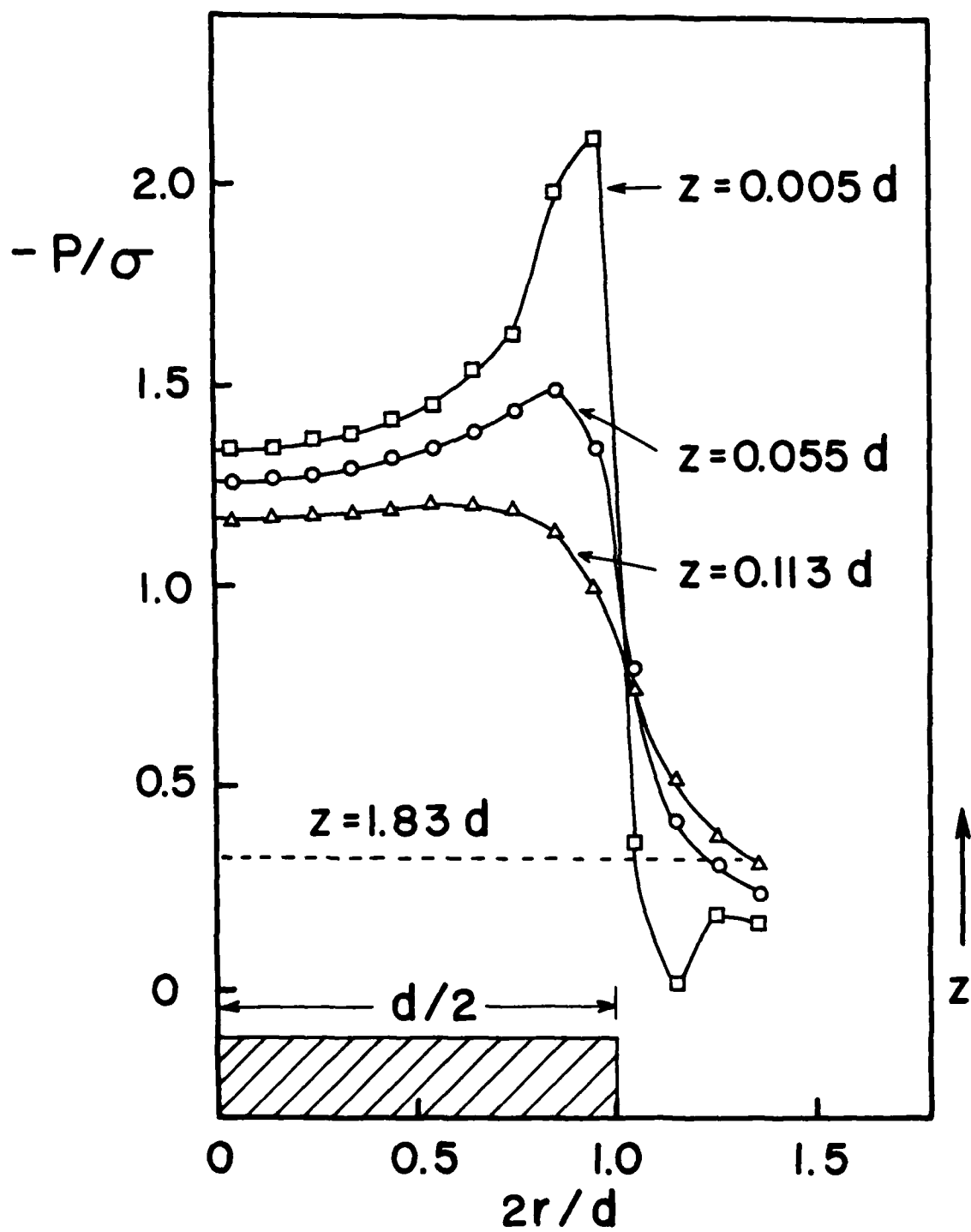


Figure 10

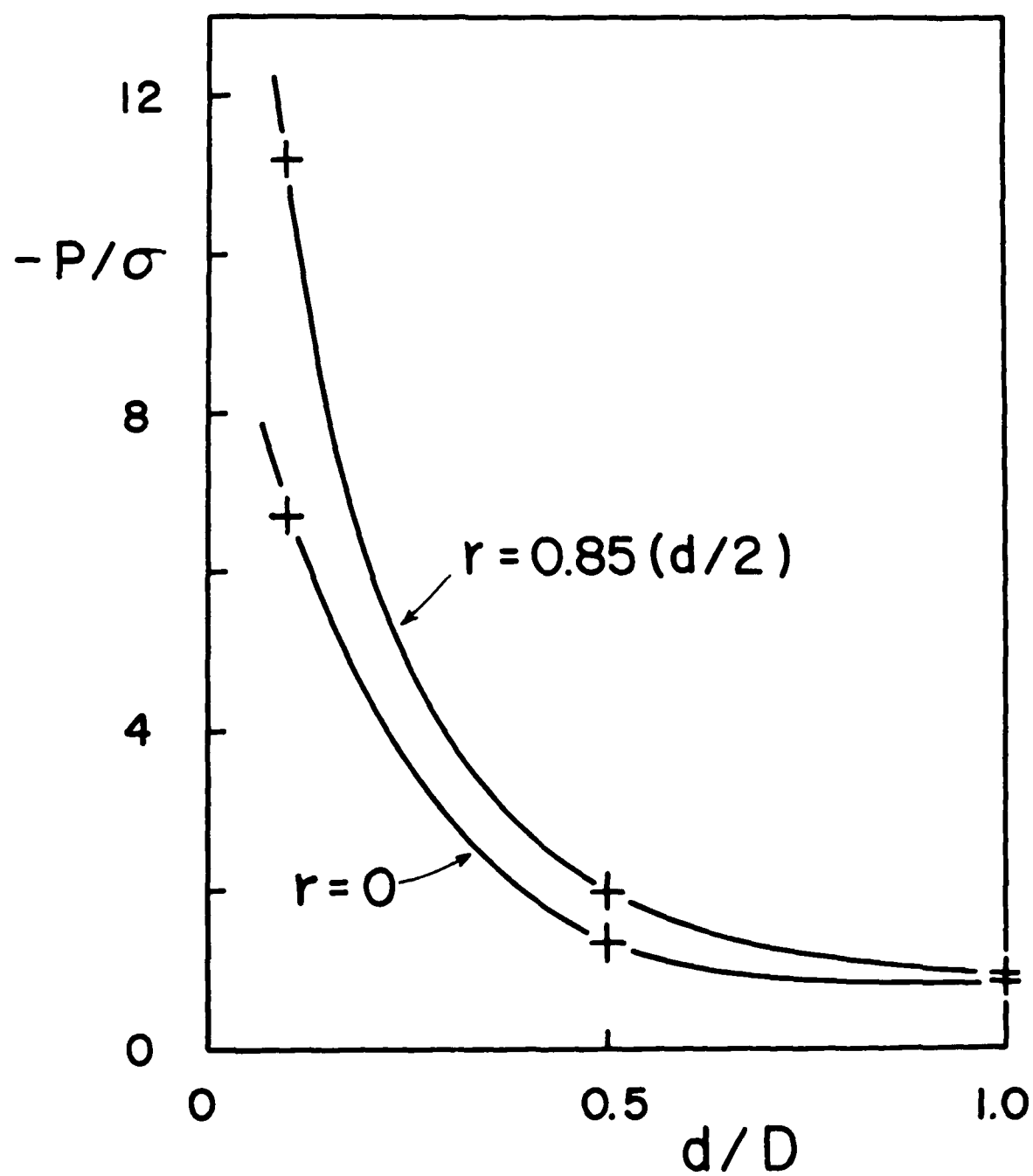


Figure 11

1500

DISTRIBUTION LIST

Dr. R.S. Miller
Office of Naval Research
Code 432P
Arlington, VA 22207
(10 copies)

Dr. J. Pastine
Naval Sea Systems Command
Code 06R
Washington, DC 20362

Dr. Kenneth D. Hartman
Hercules Aerospace Division
Hercules Incorporated
Allegheny Ballistic Lab
P.O. Box 210
Cumberland, MD 20502

Mr. Otto K. Heiney
AFATL-DLJG
Elgin AFB, FL 32542

Dr. Merrill K. King
Atlantic Research Corp.
5390 Cherokee Avenue
Alexandria, VA 22312

Dr. R.L. Lou
Aerojet Strategic Propulsion Co.
Bldg. 05025 - Dept 5400 - MS 167
P.O. Box 15699C
Sacramento, CA 95813

Dr. R. Olsen
Aerojet Strategic Propulsion Co.
Bldg. 05025 - Dept 5400 - MS 167
P.O. Box 15699C
Sacramento, CA 95813

Dr. Randy Peters
Aerojet Strategic Propulsion Co.
Bldg. 05025 - Dept 5400 - MS 167
P.O. Box 15699C
Sacramento, CA 95813

Dr. D. Mann
U.S. Army Research Office
Engineering Division
Box 12211
Research Triangle Park, NC 27709-1211

Dr. L.H. Schmidt
Office of Naval Research
Code 432P
Arlington, VA 22207

JHU Applied Physics Laboratory
ATTN: OPIA Mr. T.W. Christian
Johns Hopkins Ed.
Laurel, MD 20707

Dr. R. McGuire
Lawrence Livermore Laboratory
University of California
Code L-324
Livermore, CA 94550

P.A. Miller
736 Leavenworth Street, #6
San Francisco, CA 94109

Dr. W. Moniz
Naval Research Lab.
Code 6120
Washington, DC 20375

Dr. K.F. Mueller
Naval Surface Weapons Center
Code R11
White Oak
Silver Spring, MD 20910

Prof. M. Nicol
Dept. of Chemistry & Biochemistry
University of California
Los Angeles, CA 90024

Mr. L. Roslund
Naval Surface Weapons Center
Code R10C
White Oak, Silver Spring, MD 20910

Dr. David C. Sayles
Ballistic Missile Defense
Advanced Technology Center
P.O. Box 1500
Huntsville, AL 35807

(OYN)

DISTRIBUTION LIST

Mr. R. Geisler
ATTN: DY/MS-24
AFRPL
Edwards AFB, CA 93523

Naval Air Systems Command
ATTN: Mr. Bertram P. Sobers
NAVAIR-320G
Jefferson Plaza 1, RM 472
Washington, DC 20361

R.B. Steele
Aerojet Strategic Propulsion Co.
P.O. Box 15699C
Sacramento, CA 95813

Mr. M. Stosz
Naval Surface Weapons Center
Code R10B
White Oak
Silver Spring, MD 20910

Mr. E.S. Sutton
Thiokol Corporation
Elkton Division
P.O. Box 241
Elkton, MD 21921

Dr. Grant Thompson
Morton Thiokol, Inc.
Wasatch Division
MS 240 P.O. Box 524
Brigham City, UT 84302

Dr. R.S. Valentini
United Technologies Chemical Systems
P.O. Box 50015
San Jose, CA 95150-0015

Dr. R.F. Walker
Chief, Energetic Materials Division
DRSMC-LCE (D), B-3022
USA ARDC
Dover, NJ 07801

Dr. Janet Wall
Code 012
Director, Research Administration
Naval Postgraduate School
Monterey, CA 93943

Director
US Army Ballistic Research Lab.
ATTN: DRXBR-IBD
Aberdeen Proving Ground, MD 21005

Commander
US Army Missile Command
ATTN: DRSMI-RKL
Walter W. Wharton
Redstone Arsenal, AL 35898

Dr. Ingo W. May
Army Ballistic Research Lab.
ARRADCOM
Code DRXBR - 1BD
Aberdeen Proving Ground, MD 21005

Dr. E. Zimet
Office of Naval Technology
Code 071
Arlington, VA 22217

Dr. Ronald L. Derr
Naval Weapons Center
Code 389
China Lake, CA 93555

T. Boggs
Naval Weapons Center
Code 389
China Lake, CA 93555

Lee C. Estabrook, P.E.
Morton Thiokol, Inc.
P.O. Box 30058
Shreveport, Louisiana 71130

Dr. J.R. West
Morton Thiokol, Inc.
P.O. Box 30058
Shreveport, Louisiana 71130

Dr. D.D. Dillehay
Morton Thiokol, Inc.
Longhorn Division
Marshall, TX 75670

G.T. Bowman
Atlantic Research Corp.
7511 Wellington Road
Gainesville, VA 22065

(DYN)

DISTRIBUTION LIST

R.E. Shenton
Atlantic Research Corp.
7511 Wellington Road
Gainesville, VA 22065

Mike Barnes
Atlantic Research Corp.
7511 Wellington Road
Gainesville, VA 22065

Dr. Lionel Dickinson
Naval Explosive Ordnance
Disposal Tech. Center
Code D
Indian Head, MD 20340

Prof. J.T. Dickinson
Washington State University
Dept. of Physics 4
Pullman, WA 99164-2814

M.H. Miles
Dept. of Physics
Washington State University
Pullman, WA 99164-2814

Dr. T.F. Davidson
Vice President, Technical
Morton Thiokol, Inc.
Aerospace Group
3340 Airport Rd.
Ogden, UT 84405

Mr. J. Consaga
Naval Surface Weapons Center
Code R-16
Indian Head, MD 20640

Naval Sea Systems Command
ATTN: Mr. Charles M. Christensen
NAVSEA-62R2
Crystal Plaza, Bldg. 6, Rm 806
Washington, DC 20362

Mr. R. Beauregard
Naval Sea Systems Command
SEA 64E
Washington, DC 20362

Brian Wheatley
Atlantic Research Corp.
7511 Wellington Road
Gainesville, VA 22065

Mr. G. Edwards
Naval Sea Systems Command
Code 62R32
Washington, DC 20362

C. Dickinson
Naval Surface Weapons Center
White Oak, Code R-13
Silver Spring, MD 20910

Prof. John Deutch
MIT
Department of Chemistry
Cambridge, MA 02139

Dr. E.H. deButts
Hercules Aerospace Co.
P.O. Box 27408
Salt Lake City, UT 84127

David A. Flanigan
Director, Advanced Technology
Morton Thiokol, Inc.
Aerospace Group
3340 Airport Rd.
Ogden, UT 84405

Dr. L.H. Caveny
Air Force Office of Scientific
Research
Directorate of Aerospace Sciences
Bolling Air Force Base
Washington, DC 20332

W.G. Roger
Code 5253
Naval Ordnance Station
Indian Head, MD 20640

Dr. Donald L. Ball
Air Force Office of Scientific
Research
Directorate of Chemical &
Atmospheric Sciences
Bolling Air Force Base
Washington, DC 20332

(DYN)

DISTRIBUTION LIST

Dr. Anthony J. Matuszko
Air Force Office of Scientific Research
Directorate of Chemical & Atmospheric
Sciences
Bolling Air Force Base
Washington, DC 20332

Dr. Michael Chaykovsky
Naval Surface Weapons Center
Code R11
White Oak
Silver Spring, MD 20910

J.J. Rocchio
USA Ballistic Research Lab.
Aberdeen Proving Ground, MD 21005-5066

B. Swanson
INC-4 MS C-346
Los Alamos National Laboratory
Los Alamos, New Mexico 87545

Dr. James T. Bryant
Naval Weapons Center
Code 3205B
China Lake, CA 93555

Dr. L. Rothstein
Assistant Director
Naval Explosives Dev. Engineering Dept.
Naval Weapons Station
Yorktown, VA 23691

Dr. M.J. Kamlet
Naval Surface Weapons Center
Code R11
White Oak, Silver Spring, MD 20910

Dr. Henry Webster, III
Manager, Chemical Sciences Branch
ATTN: Code 5063
Crane, IN 47522

Dr. A.L. Slafkosky
Scientific Advisor
Commandant of the Marine Corps
Code RD-1
Washington, DC 20380

Dr. H.G. Adolph
Naval Surface Weapons Center
Code R11
White Oak
Silver Spring, MD 20910

U.S. Army Research Office
Chemical & Biological Sciences
Division
P.O. Box 12211
Research Triangle Park, NC 27709

Dr. John S. Wilkes, Jr.
FJSRL/NC
USAF Academy, CO 80840

Dr. H. Rosenwasser
AIR-320R
Naval Air Systems Command
Washington, DC 20361

Dr. Joyce J. Kaufman
The Johns Hopkins University
Department of Chemistry
Baltimore, MD 21218

Dr. A. Nielsen
Naval Weapons Center
Code 385
China Lake, CA 93555

(DYN)

DISTRIBUTION LIST

K.D. Pae
High Pressure Materials Research Lab.
Rutgers University
P.O. Box 909
Piscataway, NJ 08854

Dr. John K. Dienes
T-3, B216
Los Alamos National Lab.
P.O. Box 1663
Los Alamos, NM 87544

A.N. Gent
Institute Polymer Science
University of Akron
Akron, OH 44325

Dr. D.A. Shockey
SRI International
333 Ravenswood Ave.
Menlo Park, CA 94025

Dr. R.B. Kruse
Morton Thiokol, Inc.
Huntsville Division
Huntsville, AL 35807-7501

G. Butcher
Hercules, Inc.
P.O. Box 98
Magna, UT 84044

W. Waesche
Atlantic Research Corp.
7511 Wellington Road
Gainesville, VA 22065

Dr. R. Bernecker
Naval Surface Weapons Center
Code R13
White Oak
Silver Spring, MD 20910

Prof. Edward Price
Georgia Institute of Tech.
School of Aerospace Engineering
Atlanta, GA 30332

J.A. Birkett
Naval Ordnance Station
Code 5253K
Indian Head, MD 20640

Prof. R.W. Armstrong
University of Maryland
Dept. of Mechanical Engineering
College Park, MD 20742

Herb Richter
Code 385
Naval Weapons Center
China Lake, CA 93555

J.T. Rosenberg
SRI International
333 Ravenswood Ave.
Menlo Park, CA 94025

G.A. Zimmerman
Aerojet Tactical Systems
P.O. Box 13400
Sacramento, CA 95813

Prof. Kenneth Kuo
Pennsylvania State University
Dept. of Mechanical Engineering
University Park, PA 16802

T.L. Boggs
Naval Weapons Center
Code 3891
China Lake, CA 93555

(DYN)

DISTRIBUTION LIST

Dr. C.S. Coffey
Naval Surface Weapons Center
Code R13
White Oak
Silver Spring, MD 20910

D. Curran
SRI International
333 Ravenswood Avenue
Menlo Park, CA 94025

E.L. Throckmorton
Code SP-2731
Strategic Systems Program Office
Crystal Mall #3, RM 1048
Washington, DC 23076

R.G. Rosemeier
Brimrose Corporation
7720 Belair Road
Baltimore, MD 20742

C. Gotzmer
Naval Surface Weapons Center
Code R-11
White Oak
Silver Spring, MD 20910

G.A. Lo
3251 Hanover Street
B204 Lockheed Palo Alto Research Lab
Palo Alto, CA 94304

R.A. Schapery
Civil Engineering Department
Texas A&M University
College Station, TX 77843

Dr. Y. Gupta
Washington State University
Department of Physics
Pullman, WA 99163

J.M. Culver
Strategic Systems Projects Office
SSPO/SP-2731
Crystal Mall #3, RM 1048
Washington, DC 20376

Prof. G.D. Duvall
Washington State University
Department of Physics
Pullman, WA 99163

Dr. E. Martin
Naval Weapons Center
Code 3858
China Lake, CA 93555

Dr. M. Farber
135 W. Maple Avenue
Monrovia, CA 91016

W.L. Elban
Naval Surface Weapons Center
White Oak, Bldg. 343
Silver Spring, MD 20910

Defense Technical Information Center
Bldg. 5, Cameron Station
Alexandria, VA 22314
(12 copies)

Dr. Robert Polvani
National Bureau of Standards
Metallurgy Division
Washington, D.C. 20234

Director
Naval Research Laboratory
Attn: Code 2627
Washington, DC 20375
(6 copies)

Administrative Contracting
Officer (see contract for
address)
(1 copy)

END

5-87

DTIC